

Coupling Studies and Shielding Techniques for Electromagnetic Penetration Through Apertures on Complex Cavities and Vehicular Platforms

Eng Swee Siah, *Student Member, IEEE*, Kubilay Sertel, John L. Volakis, *Fellow, IEEE*,
Valdis V. Liepa, *Life Member, IEEE*, and Rich Wiese

Abstract—The multilevel fast multipole moment method is employed to compute the electromagnetic coupling and shielding of various aperture-coupled metallic enclosures. A phenomenological study of electromagnetic coupling, due to various slot shapes and sizes, with or without the presence of wire penetration is conducted. These slots are situated on over-moded cavities and two methods are proposed to mitigate slot coupling into the cavity's interior. As part of this work, we also investigate the coupling through similar slots and apertures within a complex platform such as an automobile. The proposed methods have shown to increase shielding by as much as 5–35 dB within the frequency range of interest.

Index Terms—Automotive electromagnetic compatibility (EMC), electromagnetic interference (EMI), method of moments (MoM), multilevel fast multipole moment method (MLFMM), numerical modeling, shielding methods.

I. INTRODUCTION

APERTURES on surfaces of metallic enclosures often serve ventilation purposes but their presence compromises the integrity of the shielding enclosure. With the possible presence of wire penetration into these cavities, the effects on shielding and wire penetration must be taken into account in electromagnetic compatibility (EMC) design. This is particularly important when analog integrated amplifier circuits are present in cavities. Often, cavity enclosures lead to amplification of the electromagnetic (EM) coupled noise at the signal port, thus creating spurious output waveforms.

In this paper, we present an analysis of overmoded slotted cavities and realistic vehicular platforms using the multilevel fast multipole moment method (MLFMM) algorithm [1]–[6]. A significant part of the paper is concerned with the development

of shielding techniques to mitigate cavity resonances. Previous analysis in EMC have employed the finite-difference time-domain (FDTD) technique [7]–[9], the method of moments (MoM) [10]–[12], the transmission-line model (TLM) method [13], [14] and the finite-element method [14], [15]. While FDTD can model a volumetric structure with rectangular cells, it generates a large number of unknowns (memory usage) and requires excessive computer time to solve. Alternatively, the MoM requires a fine mesh near a narrow slot and may also require large CPU time for multiple frequency points. To model realistic structures, we employ the MLFMM in conjunction with the MoM for multispectral frequency-domain calculations. In recent years, MLFMM has been demonstrated to require low $O(N \log N)$ memory and CPU requirements. The speed up and memory reduction associated with using MLFMM over standard MoM schemes have been shown to be 2 and 3 orders of magnitude respectively for 1 million unknowns [2], [3].

As can be expected, the analysis of slots, either in isolation, or in the presence of an enclosure, has been extensively studied [16]–[19]. Some of these studies have focused on approximate methods to estimate the coupling into the cavity interior but, in general, exact methods concentrate on the analysis of slotted enclosures mostly at lower frequencies (<1 GHz). In contrast, the focus of this paper is not on the analysis method, but rather on the understanding of the coupling mechanisms into overmoded cavities through various slot openings. The effect on EM coupling and shielding due to penetration of wire traces through apertures into the cavity interior is also investigated. A significant part of this paper focuses on relating the coupling characteristic of isolated enclosed cavities to EM coupling in the presence of a realistic automobile platform. This paper concludes with the evaluation of two innovative approaches to increase the shielding effectiveness of isolated cavities. Particular emphasis is placed on low-cost methods, potentially implementable within a system such as an automobile.

II. PHENOMENOLOGICAL STUDY

A. Analysis Validation

As a first step, it is important to validate the analysis method (see the Appendix for relevant formulation) and the pertinent computer code for the class of geometries considered. Let us, for example, consider a $30 \times 12 \times 30$ -cm rectangular cavity (see insert in Fig. 1 and Fig. 3) whose surface has an aperture of area 60 cm^2 . A rectangular aperture 20×3 cm in size and a

Manuscript received May 8, 2002; revised November 18, 2002. This work was supported in part by the U.S. Air Force Multidisciplinary University Research Project under Grant F49620-01-1-0436 and in part by the General Motors EMC Laboratory.

E. S. Siah, and V. V. Liepa are with the Radiation Laboratory, Department of Electrical Engineering and Computer Science, The University of Michigan, Ann Arbor, MI 48109-2122 USA (e-mail: esiah@engin.umich.edu; ksertel@engin.umich.edu; liepa@engin.umich.edu).

K. Sertel was with the Radiation Laboratory, Department of Electrical Engineering and Computer Science, The University of Michigan, Ann Arbor, MI 48109-2122 USA. He is now with the ElectroScience Laboratory, The Ohio State University, Columbus, OH 43210, USA.

J. L. Volakis is with the Radiation Laboratory, Department of Electrical Engineering and Computer Science, The University of Michigan, Ann Arbor, MI 48109-2122 USA, and also with the ElectroScience Laboratory, The Ohio State University, Columbus, OH 43210, USA (e-mail: volakis@engin.umich.edu).

R. Wiese is with General Motors Corporation, Milford, MI 48380 USA.

Digital Object Identifier 10.1109/TEMC.2003.810814

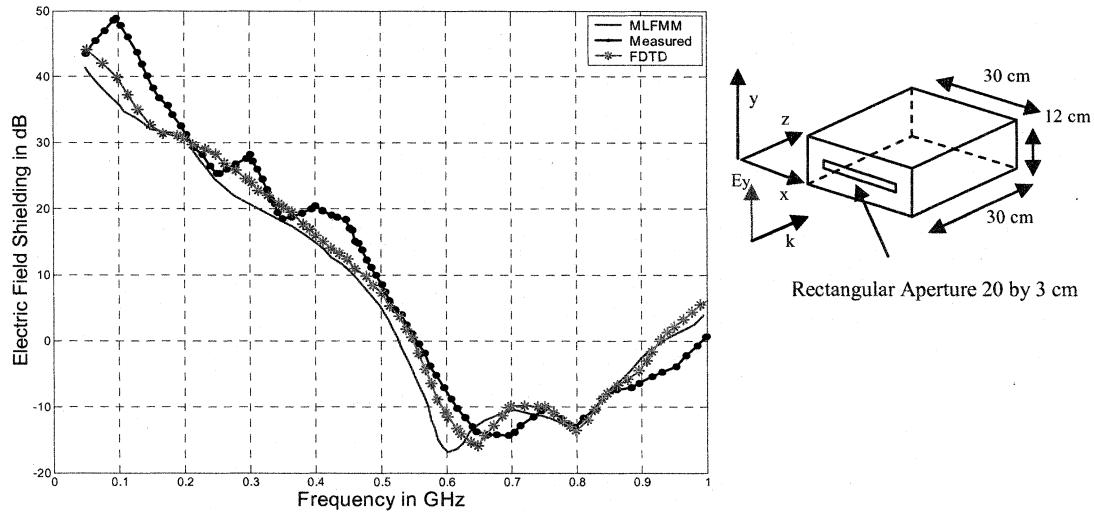


Fig. 1. Validation of the MLFMM analysis with measured data [7] and FDTD simulation for the rectangular aperture from 0.05 to 1 GHz.

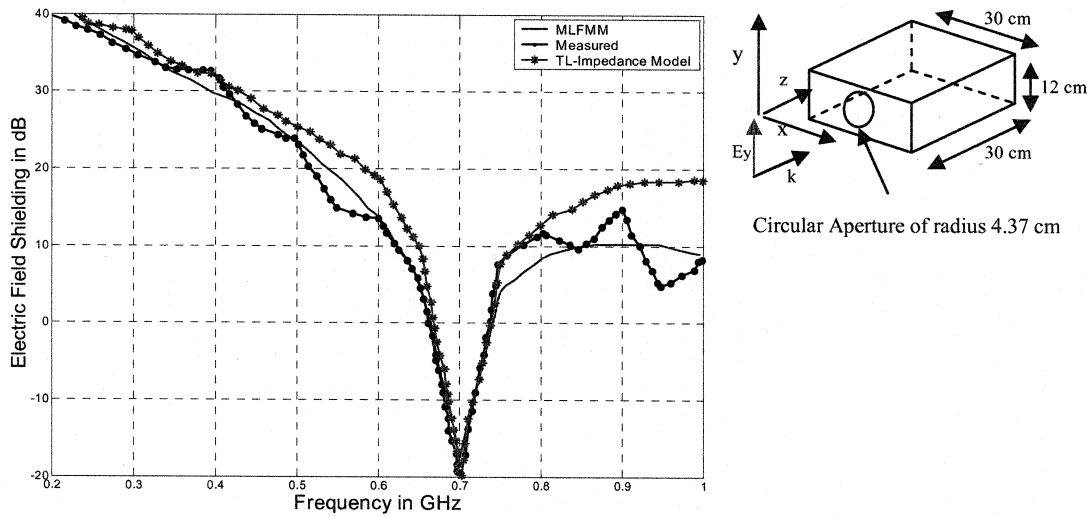


Fig. 2. Validation of the MLFMM analysis with measured data [7] and the approximate first-order transmission line model [7] from 0.2 to 1 GHz.

circular aperture of 4.37-cm radius will be considered in computing the coupled field at the center of the cavity due to an incident plane wave (incident normal to the surface of the aperture). The actual quantities to be computed throughout the paper are the electric-field shielding (EFS), the magnetic-field shielding (MFS) factor or the relative stored electric energy, respectively, given by

$$\text{EFS} = -20 \log \left(\frac{|\overline{E}^{\text{total}}|}{|\overline{E}^{\text{inc}}|} \right) \text{ dB} \quad (1)$$

$$\text{MFS} = -20 \log \left(\frac{|\overline{H}^{\text{total}}|}{|\overline{H}^{\text{inc}}|} \right) \text{ dB} \quad (2)$$

Ratio of Stored Electric Energy

$$= 10 \log \left(\frac{\iiint \epsilon_r \epsilon_o |\overline{E}^{\text{total}}|^2 \partial V}{\iiint \epsilon_r \epsilon_o |\overline{E}^{\text{inc}}|^2 \partial V} \right) \text{ dB}. \quad (3)$$

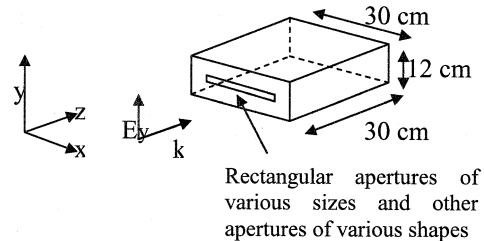


Fig. 3. Geometry of the rectangular enclosed cavity with various aperture sizes.

Here, $(\overline{E}^{\text{total}}, \overline{H}^{\text{total}})$ refer to the total fields computed at the calculation or measurement point inside of the cavity, whereas $(\overline{E}^{\text{inc}}, \overline{H}^{\text{inc}})$ refers to the incident field computed at the same location in the absence of the object/cavity.

Fig. 1 shows the computed EFS for the rectangular aperture. As seen, the MLFMM data are in good agreement with measurements and simulations based on the FDTD method [7]. In

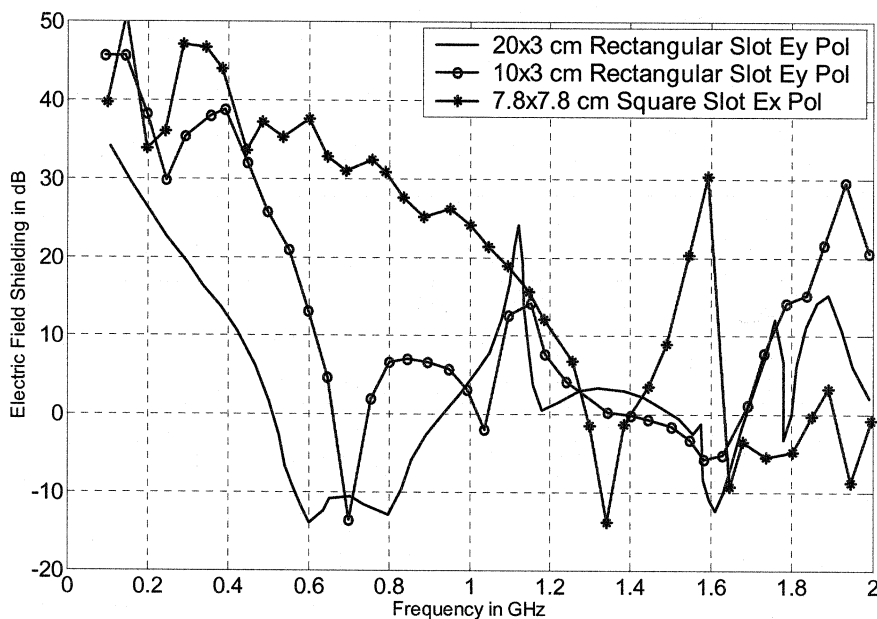


Fig. 4. EFS response for various apertures on a $30 \times 12 \times 30$ -cm rectangular enclosed cavity.

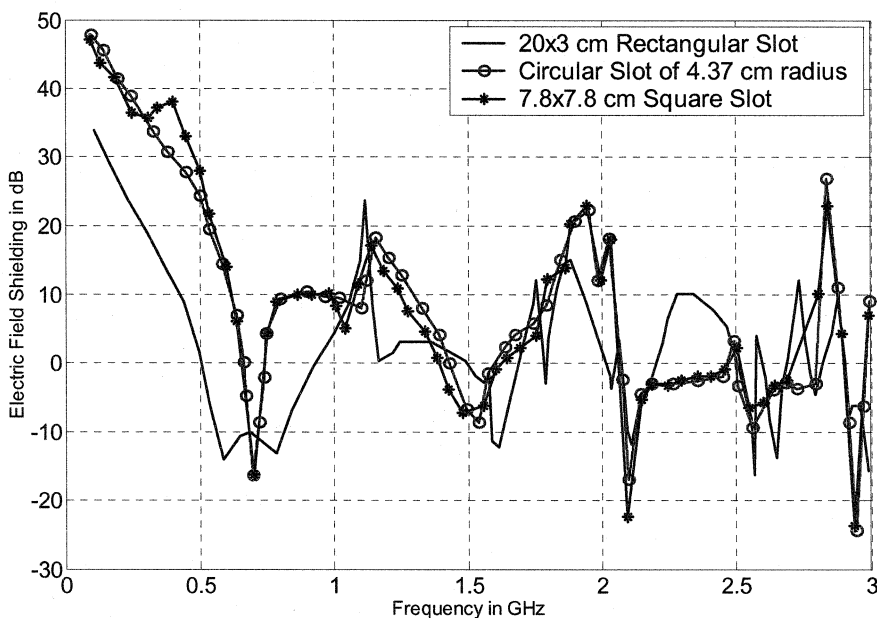


Fig. 5. EFS response for various apertures on a $30 \times 12 \times 30$ -cm rectangular cavity.

Fig. 2, we show the calculations for a circular aperture situated on the same cavity. Again, the MLFMM curve is in good agreement with the measured data [7], but the calculations based on the TLM (single mode approximation) deviate from measurements by as much as 10 dB at frequencies away from 700 MHz. The latter is the frequency where the first-cavity resonance occurs, and this can be verified from Figs. 1 and 2. However, for the rectangular slot in Fig. 1, the slot resonance at 750 MHz is close to the cavity resonance and consequently, the EFS is very poor within 500 to 900 MHz due to additional cavity–slot interactions. It is important to note that near cavity resonances, the EFS is as low as -20 dB implying a 20-dB increase from the field intensity external to the cavity. That is, the cavity res-

onances serve to significantly increase the coupled fields even through a small aperture and thus deteriorate the shielding performance of the cavity.

For the computation of the EFS in these cavities and the other following structures, the electric-field integral equation (EFIE) as prescribed in the Appendix section is used. While the EFIE exhibits some inaccuracy at the internal resonance of a completely enclosed cavity, the cavity used in these validation examples and in the following examples is not completely enclosed. For completely enclosed structures, the combined-field integral equation (CFIE) should be used for the analysis. Thus, the field value computed by the EFIE for noncompletely enclosed structures like aperture perforated cavities is accurate even at the res-

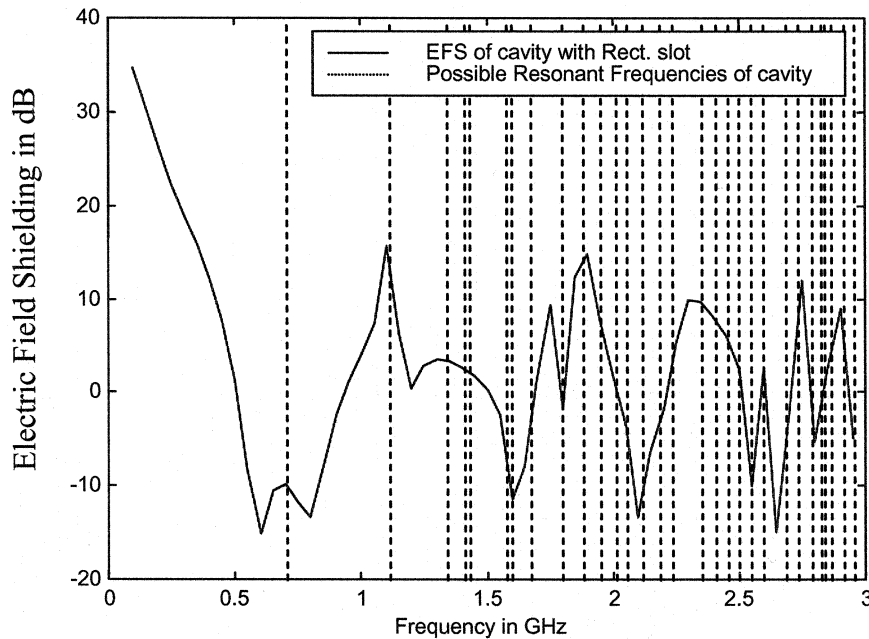


Fig. 6. Comparison of the EFS for a cavity with a rectangular slot (solid line); all possible cavity resonance frequencies are indicated with vertical dashed lines.

onance frequency and is compared to measurements and other analysis methods as shown in Figs. 1 and 2. However, the convergence of EFIE at the resonance of these cavities tends to be slow. In addition, since surface integral equations are used for the analysis methods, the surfaces of the structures are modeled with infinitely thin perfectly electrical conducting elements.

B. Different Aperture Shapes and Sizes

Having validated the MLFMM analysis, we next proceed to examine the EFS behavior of other apertures placed on the rectangular cavity (see diagram in Fig. 3). The purpose of this study is to examine the role of aperture shape on coupling behavior. Fig. 4 plots the EFS for a smaller (10×3 -cm) rectangular aperture and a 7.8×7.8 -cm-square aperture excited with horizontal polarization. The computed EFS results for the 20×3 -cm aperture are also shown for comparison.

We characteristically observe that the EFS curves vary significantly as the aperture is changed. For example, as the resonance of the slot is moved from 750 MHz to 1.5 GHz (resonance of the shorter slot), the EFS is no longer as poor around 500 to 900 MHz due to the cavity–slot interaction suppression. The fundamental resonance excited with the E_y polarized incidence at 700 MHz is associated with the TE_{101} mode. In comparison, for the square aperture with E_x polarization, the EFS is very good up to 1.3 GHz, where the higher order cavity mode TE_{011} (third vertical line in Fig. 6) is excited beyond 1.35 GHz. Obviously, for the E_x polarized excitation, the TE_{101} mode is suppressed and thus, low EFS does not occur till 1.35 GHz and greater, where we observe the interaction of the square slot resonance and higher order cavity modes.

Additional EFS curves are given in Fig. 5 for a circular (4.37-cm radius) and square (7.8×7.8 -cm) aperture of the same area as the 20×3 -cm rectangular slot, all of which are excited by the same E_y polarized plane-wave incidence. The

circular and square slots of the same area are seen to have the same EFS. However, the EFS of the circular and square slots is much higher at lower frequencies as compared to the case of an elongated rectangular slot of the same area. This is due to the shifting of the slot resonance to higher frequencies and away from the original slot resonance at 750 MHz. Thus, the former slots give rise to worse EFS than the original slot at higher frequencies where these slot resonances occur.

We surmise that the EFS is controlled by the cavity and aperture resonances. By adjusting the aperture shape and size, one can effectively control the low-frequency EFS characteristics. However, as shown in Fig. 6 (where the EFS of the cavity is compared with all its possible resonant frequencies) at higher frequencies and typically beyond the second resonance, the higher order modes are too closely packed and consequently, the EFS is almost always poor unless loading is placed interior to the cavity or at the aperture to lower the cavity Q factor. We note that typically, the frequencies corresponding to significant EM coupling coincide with the cavity resonances. This is also demonstrated in Fig. 7 where the S_{21} transmission data for a $61 \times 25.4 \times 61$ -cm cavity with a rectangular slot of 5.2×1 cm at the center of one of its faces is shown. It can be seen that at the far field, the horn antenna gives rise to an EFS (measured at the bottom of the cavity), which varies over a 20–30-dB range for enclosed cavities. If the cavity's top cover is removed, the dynamic range drops to 10–15 dB. This reduction is attributable to the removal of modal effects which in turn lower the Q factor.

We conclude this section by commenting on the field distribution within the cavity. So far, the EFS was calculated or measured at the cavity center. For these calculations to be relevant, it is important that the EFS has a smooth variation across the cavity. Fig. 8 shows the computed fields through the horizontal plane in the middle of the cavity. As seen, the field variation throughout the horizontal plane is quite consistent. That is, a higher value at the center of the cavity implies that the entire

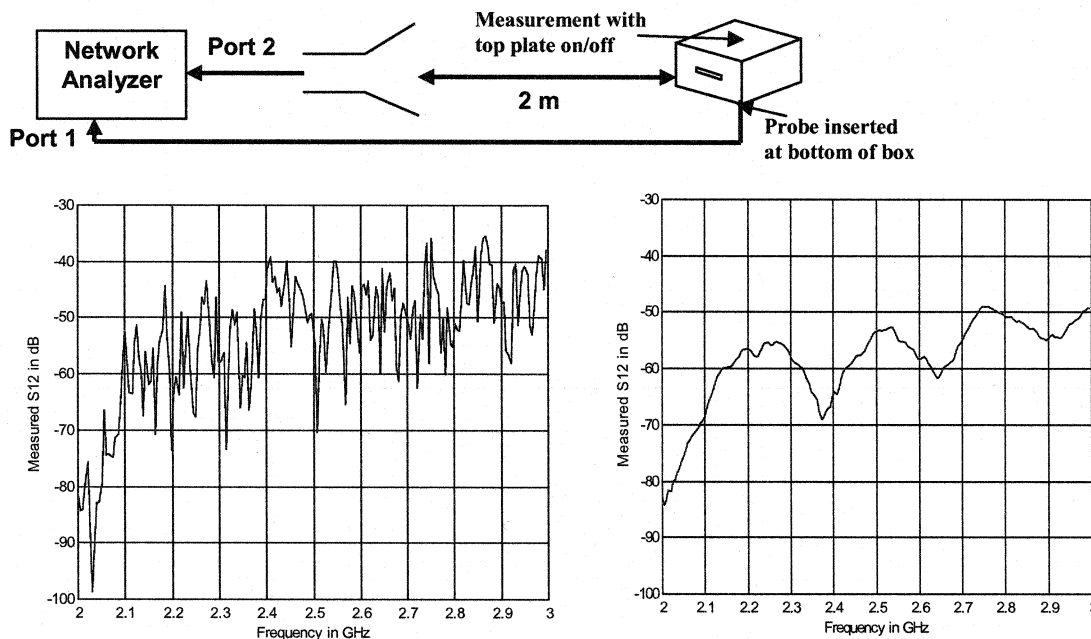


Fig. 7. Characterization of multiple resonant locations in the overmoded regime of a $61 \times 25.4 \times 61$ -cm enclosed cavity with a 5.2×1 -cm elongated rectangular slot with (a) the top cover on and (b) the top cover off.

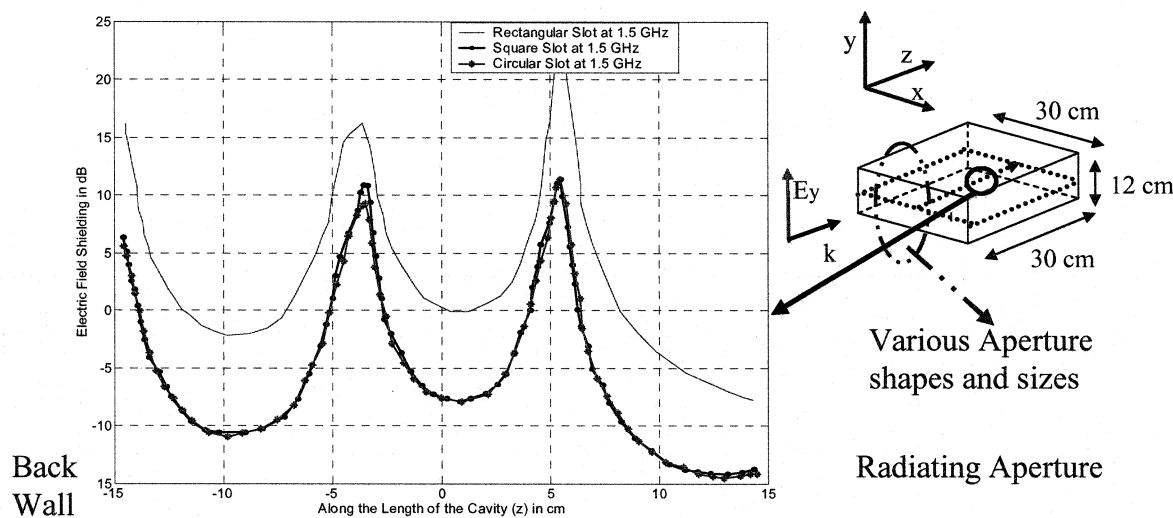


Fig. 8. Spatial distribution of the EFS for various slot apertures; EFS is measured along the cavity length (dotted line along dotted plane) and the excitation is a plane wave (at 1.5 GHz).

surface field map is shifted higher and this is demonstrated in Fig. 8.

The effect on EFS for three different slot widths or thicknesses is shown in Fig. 9. Varying the width of the elongated rectangular slot does not change the general EFS characteristics significantly (computed at the cavity center) but does change the Q factor of the response. This is attributed to the different loading associated with the various slot widths. In general, thinner slots tend to provide more shielding over a broad frequency range but exhibit larger Q factors (dynamic range of the peaks). Fig. 10 plots the stored electrical energy from (3) for the different slot widths. Although thinner slots generate higher EFS, they are associated with less electrical stored energy within the cavity volume. Conversely, thicker slots degrade the

shielding performance of the enclosed cavity but increase the stored energy within the cavity's interior.

C. Wire Penetration Through Slots Into Cavity Enclosures

Often, wires and wire bundles are placed through slot openings. Previous work in this area focused on formulating the integral equation for a wire through a slot on an infinite ground plane [20]. In this section, we are concerned with wire radiation when the wire is placed through a slot residing on a cavity surface. To better understand the wire effects on EM coupling, two different wire configurations are examined. Specifically, a straight wire through a circular slot is considered and in another case, a bent wire is placed through the slot. The straight wire is $\lambda/2$ long into the cavity, whereas the bent wire has an additional

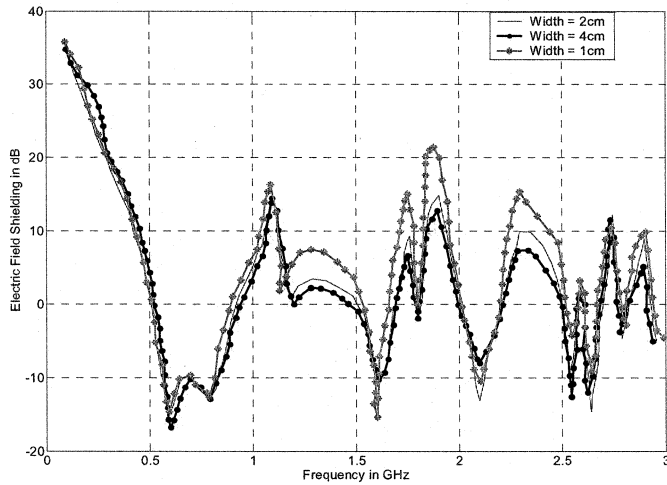


Fig. 9. EFS different rectangular slot widths.

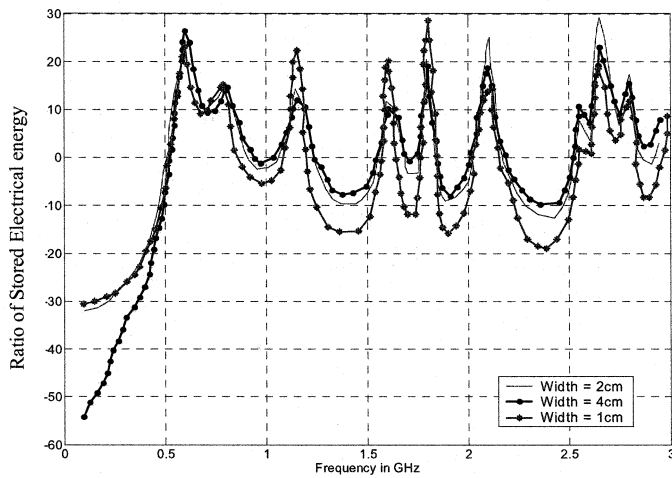


Fig. 10. Effect of different slot widths on the stored electric energy ratio.

vertical arm which extends to the bottom of the cavity. For both cases, these wires extend $\lambda/2$ (λ at 700 MHz) exterior to the cavity.

The EFS for the above two wire configurations and for a circular aperture 60 cm^2 in area is shown in Fig. 11 at 700 MHz. Characteristically, both wires deteriorate the EFS at low frequencies due to the excitation current brought by the wire into the cavity. At higher frequencies, the EFS response of the cavity is already low due to cavity resonances. However, the bent wire configuration lowers the EFS further by as much as 10 dB over certain bands. This is likely due to greater reradiation and the more consistent current flow through the longer wire. As before, the excitation is a plane wave polarized in the E_y direction and the EFS is computed at the center of the enclosed cavity.

Fig. 12 shows the stored electrical energy within the volume of the enclosed cavity. The wire's presence has a significant effect on stored energy, particularly at lower frequencies where the wire exhibits its resonance. The straight wire leads to higher stored energy up to 1 GHz whereas the bent wire exhibits higher stored energy from 1 to 2 GHz as shown in Figs. 11 and 12. Beyond 2 GHz, all the curves are in close agreement, implying that the wire shape is of less importance as the higher order

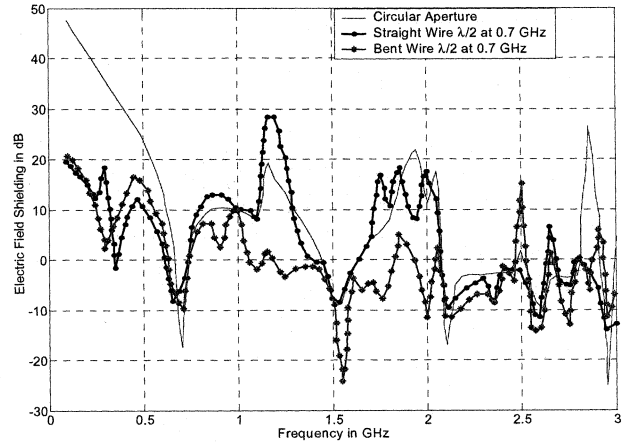
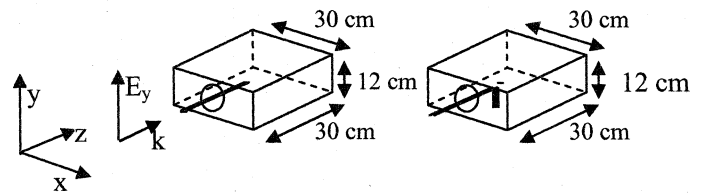


Fig. 11. Effect on EFS due to the two wire configurations with length $\lambda/2$ (λ at 0.7 GHz) interior and exterior to the cavity as shown above.

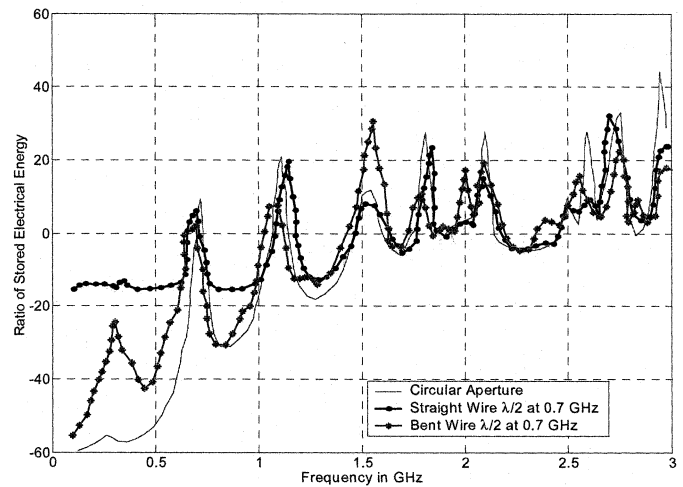


Fig. 12. Ratio of stored energy for the two-wire configurations with length $\lambda/2$ (λ at 0.7 GHz) interior and exterior to the cavity as shown above (see Fig. 11).

cavity modes dominate the field behavior within the enclosed cavity. Thus, the presence of wire elements through the slot has a significant effect on EFS at the frequency range below and near the lower order cavity modes.

The above studies clearly demonstrate that EM coupling into metallic enclosures is primarily controlled by the resonant characteristics of components comprising the structures (aperture, cavity and wires artifacts) and interactions among these.

D. Presence of Metallic Objects Within Cavity

We close this section by also examining effects of metallic artifacts or other objects placed within the original cavity. As an example, consider the same $30 \times 12 \times 30$ -cm cavity (Fig. 13) where smaller perfectly conducting (PEC) rectangular boxes of

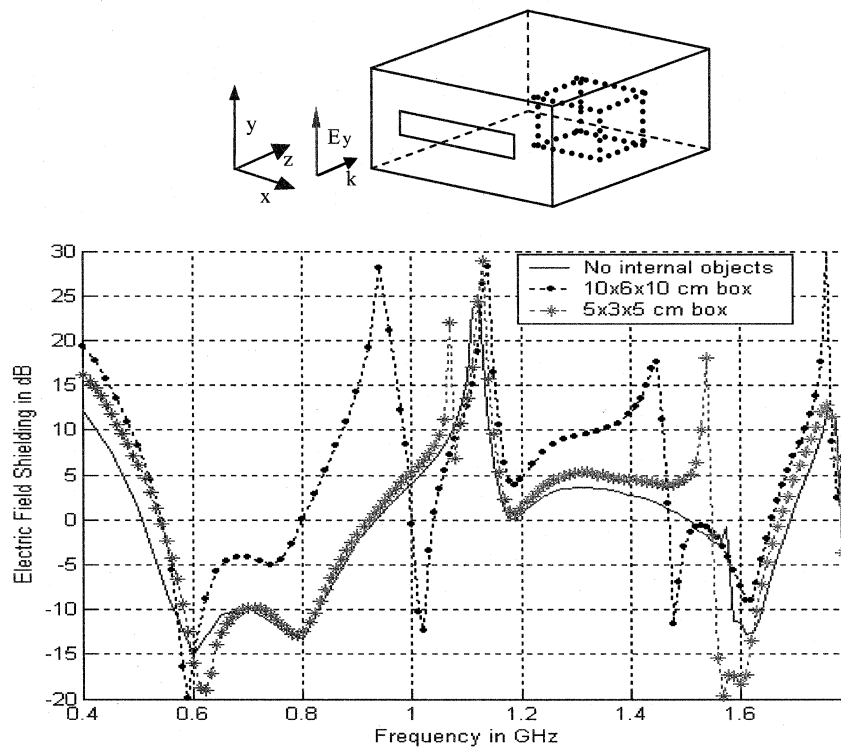


Fig. 13. EFS response of an empty cavity as compared to the cavity enclosing: 1) a $10 \times 6 \times 10$ -cm PEC box; 2) a $5 \times 3 \times 5$ -cm PEC box (shown in dotted lines).

sizes $10 \times 6 \times 10$ cm, and $5 \times 3 \times 5$ cm are placed within the cavity. Such embedded enclosures are very typical and may represent a heatsink or an electronic housing. The EFS was again computed at the center of the original cavity. In Fig. 13, we also show the EFS associated with the empty cavity for comparison. We observe that the enclosure brings additional resonances into the lower frequency range and these serve to deteriorate the cavity EFS. Such resonances correspond to the longer ray paths associated with the multibounces among the boxes within the cavity. Thus, larger Q factors may occur for larger metallic embedded boxes.

III. EMC IN PRESENCE OF VEHICULAR PLATFORM

Previous studies of EMC related to vehicular platforms have primarily focused on computing far-field antenna patterns for several antenna locations on automobiles using simplistic rectangular structures [21], [22]. On the other hand, near field EMC measurements on automobile platforms have focused on empirical experimentation and simplistic modeling [23]–[25]. In this section, we apply MLFMM analysis with curved surface elements to accurately model complex and realistic large-scale automobile platform. Specifically, we evaluate the near fields along various locations of a typical vehicle such as the General Motors GrandAM. These evaluations are useful since wire harnesses within an automobile can pickup and propagate induced spurious waveforms from ambient radiation. In addition, the propagation of these spurious waveforms to electronics packages poses a challenge to the proper functionality of the electronic device. We remark that such electronics packages are in-

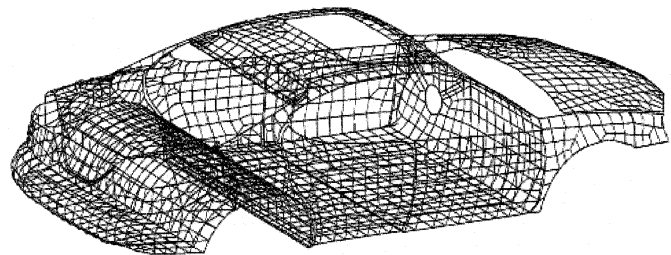


Fig. 14. Geometry of a realistic automobile platform (General Motors Grandam).

creasingly found on other platforms such as airplanes, where the proper functionality of these devices is extremely critical.

Fig. 14 presents the geometry and mesh structure consisting of quadrilateral biquadratic curvilinear elements for a typical automobile. The total length of the structure is 4.736 m, the width is about 1.75 m, while the height (from roof to power train) is about 1.1 m. At 1.475 GHz, 38 980 unknowns were used to grid the structure and the MLFMM required about 450 MB and 24 287 s of CPU time on a single SGI workstation. Using the surface currents on the curved PEC elements, the EFS at various locations within the car chassis were calculated for various plane-wave illuminations and specific antenna locations.

The EFS plots were evaluated for two lines (dotted and dot-dash lines in Fig. 15) within a plane of points (shown by dot-dot-dash lines in Fig. 15) in the passenger compartment. These curves show that the EFS is lowest in the rear of the passenger compartment for rear incidence. Also, the EFS is lowest in the front passenger compartment for front incidence. This behavior is attributed to the shadowing of the rear (front)

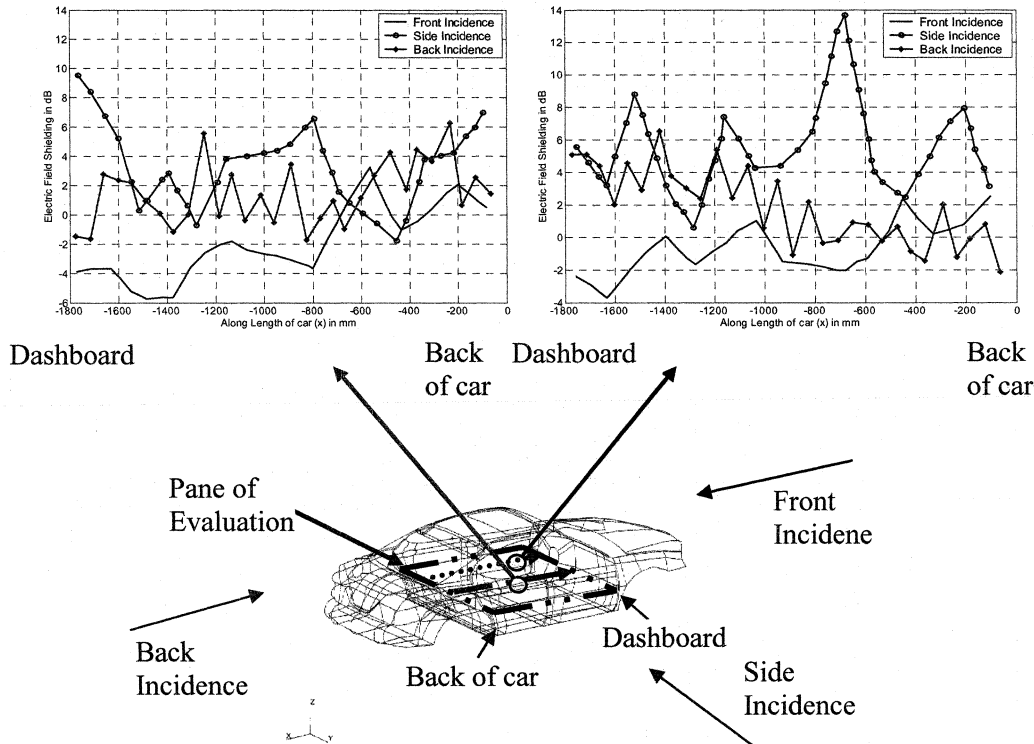


Fig. 15. EFS evaluated at two lines (dotted and dash-dot) along a plane within the passenger compartment of the car chassis for front, back, and side plane-wave incidence.

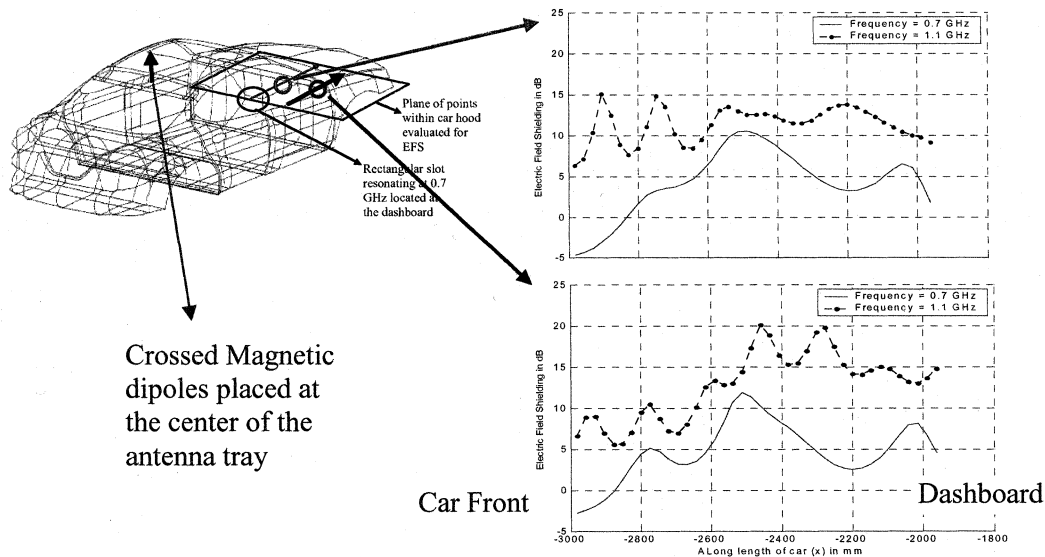


Fig. 16. EFS response evaluated within the engine compartment: radiation is due to a crossed magnetic dipole antenna through a slot resonant at 0.7 GHz on the car's dashboard.

section of the compartment for rear (front) incidence and to multibounces from the vertical panels of the illuminated sections as well as apertures residing on these panels. We note that the EFS is relatively higher for side incidence due to nonresonating apertures along the side of the automobile at 1.475 GHz. The correspondence between these results and that of apertures in an isolated enclosed cavity (see previous section) is quite apparent.

Next, we investigate the case of antenna to slot coupling on the same automobile platform. Our goal is to observe the ef-

fect of slot resonances on EFS and compare the results to those of isolated cavities. The antenna excitation is placed at the rear center of the automobile and is modeled as a pair of crossed magnetic dipoles with orthogonal phase current feeding to generate a circularly polarized field. A rectangular slot resonating at 0.7 GHz is also placed at the front dashboard of the car. Fig. 16 illustrates the computed EFS in the engine compartment of the automobile at 0.7 GHz (the 1st resonant frequency of the slot) and at 1.1 GHz (where the slot is nonresonant). Clearly, when the antenna is operating at the slot resonance (0.7 GHz), the cou-

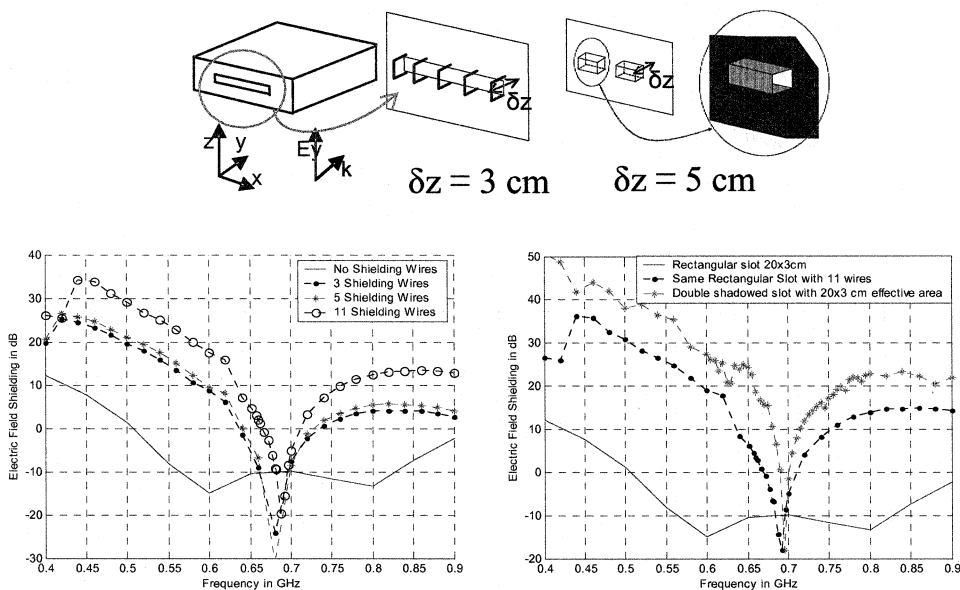


Fig. 17. EFS response of two shielding techniques: shielding wires (approach 3) and plate shadowing (approach 4).

pling into the engine compartment is much stronger (as much as 10 dB), degrading the shielding as compared to the case when the antenna is operating at 1.1 GHz. The correspondence between this case and that of apertures in an enclosed cavity can still be observed even though the automobile's engine compartment is very much an open structure.

IV. COUPLING MITIGATION TECHNIQUES

In the previous sections, we demonstrated that coupling of slots and other geometries into cavities poses a challenge to the proper functionality of electronics housed within the geometry. It is thus desirable to increase the shielding of an enclosed cavity, without compromising the aperture's ventilation. This can be done by employing some material loading across the slot or lossy material loading within the cavity. However, this is not a viable option if the slot is used for ventilation and it is further a more costly alternative. In this paper, we consider slot shielding approaches to increase the EFS subject to the following constraints: 1) maintain the same or greater aperture ventilation area; 2) low-cost modification without use of nonmetallic materials.

Several slot shielding approaches were considered using our MLFMM analysis [1]–[6]. As noted earlier, several studies have been carried out for slotted structures [16]–[18]. However, these studies have primarily focused at lower frequencies (<1 GHz). Our emphasis here is on the development of broadband shielding techniques addressing the suppression of the induced signal even when the slot and cavity resonances are close to each other (worst case). Among the low-cost shielding approaches considered are: 1) use of a short waveguide section behind the slot with a cut-off frequency above the slot/cavity resonance; 2) use of a short tortuous waveguide sections in front/behind the slot; 3) use of a wire array across the slot to attenuate and perturb slot resonances; 4) use of plate shielding (slot shadowing) with side apertures maintaining the same

ventilation area as the original slot. Among these methods, method 1) was effective only if the waveguide section was greater than $\lambda/2$ in length, making it impractical for our purposes. Further, method 2) did not improve shielding as the tortuous waveguide still allowed significant leakage near the modal cavity resonances. In contrast, the latter two shielding methods were found to be more useful over a larger bandwidth.

The EFS responses for the latter two shielding approaches, methods 3) and 4) used for the same rectangular slot is shown in Fig. 17. As seen, using 11 or more shielding wires at a distance of 3 cm from the slot face improves the shielding performance by as much as 5 to 25 dB over a broad frequency range. However, at the resonance around 0.7 GHz, the EFS continues to be low but over a very narrow frequency range. To increase the EFS at this frequency range, we considered method 4), *viz.* that of using a shielding plate behind or in front of the slot as shown to the right of Fig. 17. To ensure that ventilation is maintained, the total aperture area of the double slot shadowing method is kept the same to the original 20×3 -cm elongated rectangular slot. As can be seen, this shadowing has further improved shielding. Moreover, it narrowed the EFS dip at the cavity resonance. In effect, the shadowing plate [method 4)] improved the EFS by 5–35 dB over the entire bandwidth considered here. Both of the latter shielding methods also served to shift the slot resonance away from the cavity resonance. Nevertheless, when operating at cavity resonances, coupling into the cavity will occur due to any aperture opening. Specifically, the dip in EFS for the latter two shielding methods is over a very narrow range of frequencies. In addition, the shielding wires and the slot shadowing has loaded the cavity with some reactive impedance, shifting the resonant frequency of the cavity slightly away from 0.7 GHz.

In Fig. 18, we show the EFS dependence on the distance (δZ) between the slot and the wire array or shielding plate. We observe that the EFS improves by about 3 dB when $\delta Z = 2$ cm as compared to larger values of δZ . Beyond $\delta Z = 3$ cm, the shielding effectiveness no longer improves significantly. For the

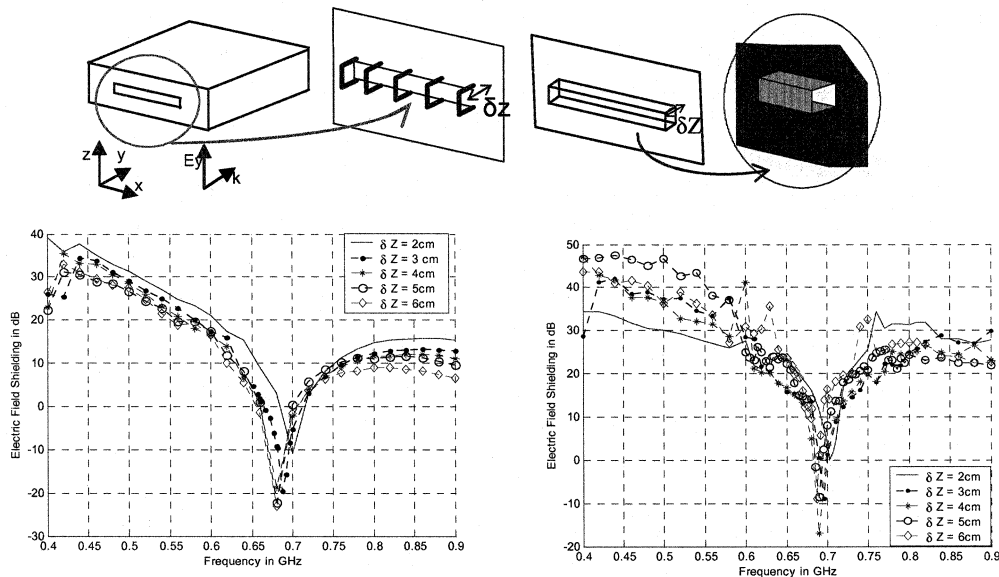


Fig. 18. Effect of varying the distance δZ of the shielding wires (10 wires) and slot shadowing plate from the slot's surface.

shadowing plate case, the optimum value of δZ was around 5 cm. From Fig. 18, we also note that this optimized value of δZ provides the best overall EFS performance, especially at lower frequencies prior to the excitation of the lowest cavity mode and reasonably good shielding above the cavity resonance. Again, as before, the array of shielding wires and the slot shadowing loads the cavity differently with different values of δZ , shifting the fundamental cavity resonant frequency slightly away from 0.7 GHz.

As a general guideline, shielding increases as more wires are placed across the aperture. However, the degree of shielding improvement reaches diminishing returns. The degree of shielding improvement also depends on the distance (δZ) of shielding wires from the slot surface. The optimal numbers of wires and the distance δZ have been prescribed in the previous paragraph. For the considered slot, the largest shielding improvement is optimal when $\delta Z = 5$ cm from the slot surface. It should be noted however, that the wire array or the employed slot shadowing technique may slightly detune the cavity enclosure and this should be factored in the design of the cavity enclosure.

V. SUMMARY AND CONCLUSIONS

In this paper, we presented an extensive study of the coupling through various slots situated either on isolated rectangular boxes or on complicated platforms such as an automobile. Various slot shapes were examined over a broad frequency range. The presence of wires through slots was considered and techniques were introduced to improve the shielding effectiveness of slot openings without compromising the ventilation area. The following is a summary of this study's conclusions.

1) Coupling through slot opening on enclosed structures is primarily controlled by the resonances of the slot openings, the cavity itself and any substructures within the enclosure. This observation is used in subsequent work to develop simple

but accurate models for coupling into enclosures through any arbitrary shape slot.

- 2) The shielding effectiveness deteriorates significantly near the structure or substructure resonances and in fact, the interior field can be as much as 20–30 dB higher within the enclosure as compared to the exterior ambient environment.
- 3) Slots situated in a vehicle can decrease the EFS by as much as 10 dB or more when an ambient illumination is operating at the resonating frequency of the slot
- 4) The presence of wires through slots causes deterioration of the EFS at lower frequencies and certainly at the resonant frequencies of these wires. The effect is further compounded when the resonant frequency of the wire coincides with the resonant frequency of the cavity.
- 5) For external plane-wave incidence, the EFS within the interior passenger compartment of a vehicle can vary over a 10–15-dB range. This is primarily due to multiple reflections between the vertical panels of the vehicle and the presence of radiating/resonant apertures on these panels.
- 6) The shielding of aperture openings on cavities can be improved by using an array of shielding wires at a distance of $\delta Z = 2$ cm in front of the aperture. This yields a 5–25-dB improvement in shielding with a very narrow dip in performance only at the resonance of the cavity.
- 7) The placement of a shielding plate in front of the slot provided the best shielding performance while maintaining the same ventilation area. This method yields as much as 5–35-dB shielding improvement by placing the plate at $\delta Z = 5$ cm in front of the slot.

APPENDIX

GENERAL FORMULATION FOR MLFMM

The EFIE for a PEC object can be written as

$$\hat{t} \cdot \int_S \left[\bar{J}(r') + \frac{1}{k^2} \nabla \cdot \bar{J}(r') \nabla \right] \frac{e^{jkR}}{R} ds' = \frac{4\pi j}{k\eta} \hat{t} \cdot \bar{E}^i(\bar{r}) \quad (\text{A1})$$

where \vec{J} represents the surface currents, \hat{t} is the unit vector tangent to the surface of the PEC, \vec{E}^i is the incident electric field, η denotes the free space impedance and k refers to the wavenumber. Alternatively, one could employ the magnetic-field integral equation (MFIE)

$$T[\hat{n} \times \vec{J}(r')] + \int_S \vec{J}(r') \times \nabla \left(\frac{e^{jkR}}{4\pi R} \right) ds' = \frac{\eta}{k} \vec{H}^i(\vec{r}) \quad (\text{A2})$$

valid for closed structures. In both (A1) and (A2), $R = |\vec{r} - \vec{r}'|$ is a vector from the source \vec{r}' to the observation point \vec{r} and the parameter $T = 1 - \Omega/4\pi$, where Ω is the exterior solid angle subtended by the pair of quadrilateral patches at their junction. For points away from the surface of the conducting surface, (A2) and (A1) are modified as follows:

$$\int_S \vec{J}(r') \times \nabla \left(\frac{e^{jkR}}{R} \right) ds' = \frac{4\pi\eta}{k} \vec{H}^s(r) \quad (\text{A3})$$

$$\int_S \left[\vec{J}(r') + \frac{1}{k^2} \nabla' \cdot \vec{J}(r') \nabla \right] \frac{e^{jkR}}{R} ds' = \frac{4\pi j}{k\eta} \vec{E}^s(\vec{r}) \quad (\text{A4})$$

where $\vec{H}^s(r)$ and $\vec{E}^s(r)$ denote the scattered fields away from the conducting surface. The unknown currents $\vec{J}(r')$ in (A1) can be solved using the standard MoM technique by expanding the current as a sum of N known basis functions $\vec{j}_i(r')$, *viz.*,

$$\vec{J}(r') \approx \sum_{i=1}^N a_i \vec{j}_i(r'). \quad (\text{A5})$$

Substituting this expansion in the EFIE (A1) yields

$$\sum_{i=1}^N a_i \hat{t} \cdot \int_S \left[\vec{j}_i(r') + \frac{1}{k^2} \nabla' \cdot \vec{j}_i(r') \nabla \right] \frac{e^{jkR}}{R} ds' \approx \frac{4\pi j}{k\eta} \hat{t} \cdot \vec{E}^i(r) \quad (\text{A6})$$

where \hat{t} denotes the vector tangent to the surface a_i are the unknown coefficients to be found by solving (A6). These unknown coefficients of the current expansion are found via Galerkin's method leading to the linear system of equations

$$\sum_{i=1}^N Z_{mi} a_i = b_m; \quad [Z] \{a\} = \{b\}, \quad m = 1, 2, \dots, N \quad (\text{A7})$$

$$Z_{mi} = \hat{t} \cdot \int_s \vec{t}_m(r) ds \cdot \int_{s'} \left[\vec{j}_i(r') + \frac{1}{k^2} \nabla' \cdot \vec{j}_i(r') \nabla \right] \cdot \frac{e^{jkR}}{R} ds' \quad (\text{A8})$$

$$b_m = \frac{4\pi j}{K\eta} \hat{t} \cdot \int_s \vec{t}_m(r) \cdot \vec{E}^i(\vec{r}) ds \quad (\text{A9})$$

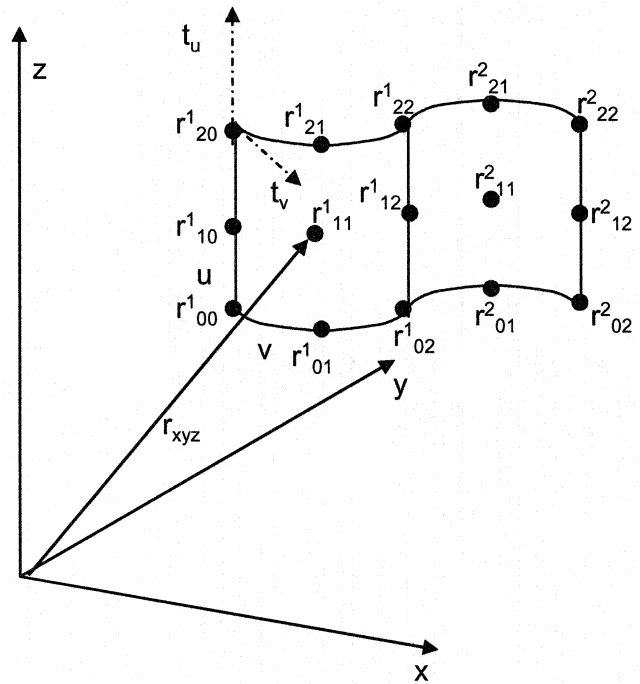


Fig. 19. Geometrical representation of the biquadratic curvilinear quad patch element (pair of connected patches is shown).

where $\vec{t}_m(r)$ is the employed testing function. For Galerkin's testing, this function is set equal to the basis functions $\vec{j}_i(r)$.

When employing the MLFMM, a spherical (multipole) wave expansion of the free-space Green's function for carrying out the matrix-vector products in an iterative solution of the linear system (A7). The associated details of the implementation are given in the literature [3]–[5]. The multilevel aspect of the MLFMM algorithm is implemented using a multilevel nested group strategy and clustering of the basis functions with the k means algorithm [26]. Typically, the conjugate gradient squared iterative method is used to solve for $\{a_i\}$. In addition, for fast multispectral analysis, the solution of the previous frequency point is used as the starting iterate for the next frequency point.

Of particular importance in our implementation is the use of curvilinear elements to discretize the geometry surfaces [6]–[9]. This increases the accuracy of modeling curved surface geometries and alleviates the need for higher spatial sampling. In our case, curved quadrilateral biquadratic surface elements are used to model complicated geometries. A quadrilateral biquadratic surface patch (Fig. 19) is defined by nine node points in terms of two mathematical parameters u and v

$$r(u, v) = \sum_{i=0}^2 \sum_{j=0}^2 a_{ij} u^i v^j, \quad 0 < u < 1 \text{ and } 0 < v < 1. \quad (\text{A10})$$

The coefficients a_{ij} are determined from the relation $r(u_i, v_j) = r(x_n, y_n, z_n)$, where $r(x_n, y_n, z_n)$ is the distance to a particular node point on the patch (see dots in Fig. 19) from the defined origin. Each curved surface patch element pair supports a curved rooftop basis function with each edge of the patch supporting one half of the curved basis function. Thus, four

edge-based rooftop basis functions are used to represent the current density on a curved patch and these are given by

$$\begin{aligned}\bar{f}_u^{(1)} &= \frac{u}{\sqrt{g}}\bar{t}_u, & \bar{f}_u^{(2)} &= \frac{(1-u)}{\sqrt{g}}\bar{t}_u, & \bar{f}_v^{(1)} &= \frac{v}{\sqrt{g}}\bar{t}_v, \\ \bar{f}_v^{(2)} &= \frac{(1-v)}{\sqrt{g}}\bar{t}_v\end{aligned}\quad (\text{A11})$$

where g is the determinant of the metric tensor given by (A10) and \bar{t}_u and \bar{t}_v are the two principle tangent vectors on the surface of the curved patch element in the u and v axis, respectively. The basis $\bar{f}_u^{(1)}$ represents one half of the basis function whereas $\bar{f}_u^{(2)}$ represents the other half of the basis function in (A5) along the u axis. Similarly, $\bar{f}_v^{(1)}$ and $\bar{f}_v^{(2)}$ represent the respective one half of the basis function in (A5) along the v axis (see Fig. 19). The superscripts of the node points in Fig. 19 refer to the quad patch element number whereas the subscripts refer to the (u_i, v_j) points of the patch. For two neighboring patches with continuous current flow along a common edge, the corresponding nodes along the common edge must be the same to both patches.

The presence of g in (A11) further serves as a normalization factor and ensures that the current continuity boundary condition is satisfied across neighboring patches.

REFERENCES

- [1] T. F. Eibert, K. Sertel, and J. L. Volakis, "Hybrid finite element modeling of conformal antenna and array structures utilizing fast integral methods," *Int. J. Numer. Model.*, vol. 13, pp. 2–3, 2000.
- [2] K. Sertel and J. L. Volakis, "Incomplete ILU Preconditioner for Fast Multipole Method (FMM)," *Microwave Opt. Tech. Lett.*, vol. 28, pp. 265–267, 20, 2000.
- [3] —, "Multilevel fast multipole method implementation using parametric surface modeling," in *Dig. IEEE Int. Symp. Antennas Propagation Soc.*, vol. 4, 2000, pp. 1852–1855.
- [4] R. Coifman, V. Rokhlin, and S. Wandzura, "The fast multipole method for the wave equation: A pedestrian prescription," *IEEE Antennas Propag. Mag.*, vol. 35, pp. 7–12, June 1993.
- [5] J. M. Song, C. C. Lu, and W. C. Chew, "Multilevel fast multipole algorithm for electromagnetic scattering by large complex objects," *IEEE Trans. Antennas Propag.*, vol. 45, pp. 1488–1493, Oct. 1997.
- [6] K. Sertel and L. Gurel, "A comparisons of surface modeling techniques," in *Dig. IEEE Int. Symp. Antennas Propagation Soc.*, vol. 3, July 1997, pp. 1834–1837.
- [7] M. P. Robinson, T. M. Benson, C. Christopoulos, J. F. Dawson, M. D. Ganley, A. C. Marvin, S. J. Porter, and D. W. P. Thomas, "Analytical formulation for the shielding effectiveness of enclosures with apertures," *IEEE Trans. Electromagn. Compat.*, vol. 40, pp. 240–248, Aug. 1998.
- [8] M. Lin, J. Nuebel, J. L. Drewniak, R. E. DuBroff, T. H. Hubing, and T. P. V. Doren, "EMI from cavity modes of shielding enclosures—FDTD modeling and measurements," *IEEE Trans. Electromagn. Compat.*, vol. 42, pp. 29–38, Feb. 2000.
- [9] J. Mix, G. Haussmann, M. Picket-May, and K. Thomas, "EMC/EMI design and analysis using FDTD," in *Proc. IEEE Int. Symp. Electromagnetic Compatibility*, vol. 1, 1998, pp. 177–181.
- [10] F. Olyslager, E. Laermans, D. De Zutter, S. Criel, R. De Smedt, and A. De Clercq, "Numerical and experimental study of the shielding effectiveness of a metallic enclosure," *IEEE Trans. Electromagn. Compat.*, vol. 41, pp. 202–213, Aug. 1999.
- [11] W. Wallyn, D. De Zutter, and H. Rogier, "Prediction of the shielding and resonant behavior of multisection enclosures based on magnetic current modeling," *IEEE Trans. Electromagn. Compat.*, vol. 44, pp. 130–138, Feb. 2002.
- [12] G. Cerri, R. D. Leo, and V. M. Primiani, "Theoretical and experimental evaluation of the electromagnetic radiation from apertures in shielded enclosures," *IEEE Trans. Electromagn. Compat.*, vol. 34, pp. 423–432, Nov. 1992.
- [13] C. Christopoulos, "Application of the TLM method to equipment shielding problems," in *Proc. IEEE Int. Symp. Electromagnetic Compatibility*, vol. 1, 1998, pp. 188–193.
- [14] W. P. Carpes, G. S. Ferreira, A. Raizer, L. Pichon, and A. Razeq, "TLM and FEM methods applied in the analysis of electromagnetic coupling," *IEEE Trans. Magn.*, vol. 36, pp. 982–985, Apr. 2000.
- [15] J. L. Volakis, A. Chatterjee, and L. C. Kempel, *Finite Element Method for Electromagnetics*. New York: IEEE Press, 1998.
- [16] C. M. Butler, Y. Rahmat-Samii, and R. Mittra, "Electromagnetic penetration through apertures in conducting surfaces," *IEEE Trans. Antennas Propag.*, vol. AP-26, pp. 291–302, Jan. 1978.
- [17] R. F. Harrington, "Resonant behavior of a small aperture backed by a conducting body," *IEEE Trans. Antennas Propag.*, vol. AP-30, pp. 205–212, Mar. 1982.
- [18] C. H. Liang and D. K. Cheng, "Electromagnetic fields coupled into a cavity with a slot-aperture under resonant conditions," *IEEE Trans. Antennas Propag.*, vol. AP-30, pp. 664–672, July 1982.
- [19] M. Lin, J. L. Drewniak, S. Radu, J. Nuebel, T. H. Hubing, R. E. DuBroff, and T. P. Van Doren, "An EMI estimate for shielding-enclosure evaluation," *IEEE Trans. Electromagn. Compat.*, vol. 43, pp. 295–304, Aug. 2001.
- [20] C. M. Butler and K. R. Umashankar, "Electromagnetic excitation of a wire through an aperture-perforated conducting screen," *IEEE Trans. Antennas Propag.*, vol. AP-24, pp. 456–462, July 1976.
- [21] R. Abou-Jaoude and E. K. Walton, "Numerical modeling of on-glass conformal automobile antennas," *IEEE Trans. Antennas Propag.*, vol. 46, pp. 845–852, June 1998.
- [22] E. K. Walton, R. Abou-Jaoude, and M. E. Pekar, "Annular slot windshield antenna," *IEEE Trans. Veh. Technol.*, vol. 47, pp. 765–773, Aug. 1998.
- [23] I. E. Noble, "Electromagnetic compatibility in the automotive environment," *Proc. IEEE—Sci., Meas. Technol.*, vol. 141, 1994.
- [24] R. Ball, P. Jennings, and P. Lever, "EMC testing Rover cars," *Eng. Sci. Educ. J.*, vol. 1, no. 6, 1992.
- [25] J. L. Herring and C. Christopoulos, "The vehicle body as an electromagnetic shield-numerical simulation for emission and susceptibility studies," in *Proc. 7th Int. Conf. Electromagnetic Compatibility*, 1990, pp. 125–131.
- [26] P. Griffiths and I. D. Hill, *Applied Statistics Algorithms*. West Sussex, U.K.: Ellis Horwood, 1985.

Eng Swee Siah (S'99) was born on August 12, 1974, in Singapore. He received the B.Eng. degree, with first class honors, from the National University of Singapore, Singapore, and the M.Sc. degree in electrical engineering from The University of Michigan, Ann Arbor, in July 1999, and August 2002, respectively. He is currently working toward the Ph.D. degree in electrical engineering and computer science at The University of Michigan.

He is currently a Graduate Student Research Assistant at the Electrical Engineering and Computer Science Department, The University of Michigan. From October 1999 to July 2000, he participated in the graduate program in communications engineering and signal processing at the Technical University of Munich, Munich, Germany. His research interests include electromagnetic theory, computational electromagnetics, fast and hybrid electromagnetic methods, electromagnetic compatibility and interference, antenna design, and analysis and EM optimization.

Kubilay Sertel was born on June 27, 1973, in Tekirdag, Turkey. He received the B.S. degree from the Middle East Technical University, Ankara, Turkey, and the M.S. degree from Bilkent University, Ankara, Turkey, in 1995 and 1997, respectively. He is currently working toward the Ph.D. degree in electrical engineering and computer science at The Ohio State University, Columbus.

He was a Research Assistant at Bilkent University, and a Graduate Student Research Assistant in the Radiation Laboratory, Electrical Engineering and Computer Science Department, The University of Michigan, Ann Arbor. He is currently with the Electroscience Laboratory, The Ohio State University, Columbus. His research areas include electromagnetic theory, computational electromagnetics, integral equation and hybrid methods, fast and efficient methods for large-scale electromagnetics problems, and parallel implementations of fast algorithms.